



One-pot fabrication of $\text{Bi}_3\text{O}_4\text{Cl}/\text{BiOCl}$ plate-on-plate heterojunction with enhanced visible-light photocatalytic activity

Shangbo Ning, Luyao Ding, Zheguan Lin, Qianying Lin, Hualei Zhang, Huaxiang Lin*, Jinlin Long, Xuxu Wang*

Research Institute of Photocatalysis, State Key Laboratory of Photocatalysis on Energy and Environment, Fuzhou University, Fuzhou 350002, PR China



ARTICLE INFO

Article history:

Received 19 October 2015

Received in revised form

11 December 2015

Accepted 11 December 2015

Available online 14 December 2015

Keyword:

$\text{Bi}_3\text{O}_4\text{Cl}/\text{BiOCl}$

Heterostructure

Visible light

Photocatalysis

Orange II

ABSTRACT

$\text{Bi}_3\text{O}_4\text{Cl}/\text{BiOCl}$ ($\text{B}_3\text{O}_4\text{C}/\text{BOC}$) heterojunction photocatalyst with high visible-light photocatalytic activity was synthesized by one-pot hydrothermal method. The morphology, crystal, structure, optical and photocatalytic property of the synthesized samples were characterized by XRD, SEM, HRTEM, EDX, BET, UV-vis DRS, photocurrent, PL, and etc. The $\text{B}_3\text{O}_4\text{C}/\text{BOC}$ heterojunction photocatalyst exhibited higher photocatalytic activity than pure BiOCl (BOC) and $\text{Bi}_3\text{O}_4\text{Cl}$ ($\text{B}_3\text{O}_4\text{C}$) for the degradation of Orange II under visible light ($\lambda \geq 420$ nm). The 0.50 $\text{B}_3\text{O}_4\text{C}/\text{BOC}$ -1 heterojunction exhibited the highest photocatalytic activity and its photocatalytic efficiency was 4.4-fold more than those of pure BOC . In addition, the 0.50 $\text{B}_3\text{O}_4\text{C}/\text{BOC}$ -1 synthesized by one-pot hydrothermal method exhibited higher photocatalytic activity than that prepared by two-step traditional synthesis method. The enhanced photocatalytic activity of the $\text{B}_3\text{O}_4\text{C}/\text{BOC}$ heterostructure photocatalyst was predominantly attributed to the efficient separation of photoinduced electrons and holes. Ultimately, the results also reveal that $\cdot\text{OH}$ and $\cdot\text{O}^{2-}$ radicals are primarily reactive species in the photocatalytic system, which are the key factors responsible for the nearly complete mineralization of Orange II.

© 2015 Elsevier B.V. All rights reserved.

1. Introduction

In recent decades, as a promising environmental-friendly technology for organic pollutant remediation and the conversion of solar energy into chemical energy, heterogeneous semiconductor photocatalysis TiO_2 attracts augmenting attention [1–3]. Although TiO_2 is emerging as a widely applied field, there are some existent problems associated with photocatalysts. The two main limitations are that: (1) the large bandgap, however, TiO_2 ($E_g = 3.2$ eV) can utilize only the photons in the UV region ($\lambda \leq 380$ nm), which limits the application of TiO_2 indoor or in solar light. (2) the high recombination rate of photoinduced hole-electron that hampers the photocatalytic efficiency [4]. To solve the above mentioned problems, developing novel and efficient visible-light-active photocatalysts is still a great challenge for material scientists and researchers worldwide.

Recently, BOC has become one of the most commonly used photocatalysts, which exhibits more efficient photocatalytic activity than TiO_2 because of their open crystalline structure [5–8].

The open crystalline structure has a layered Sillén–Aurivillius related oxide-structure consisting of $[\text{Bi}_2\text{O}_2]$ layers sandwiched between two slabs of $[\text{Cl}]$ ions [9] that may ensure itself with the self-built internal static electric fields. The internal static electric fields in BOC can prompt the separation and transportation of photo-generated electron and hole. However, BOC still faces the same challenges as TiO_2 , which is limited by light absorption and large energy loss [10]. Until now, more efforts have been made to improve the photocatalytic activity of the pristine catalyst by controlling the selected orientation of crystal growth [11], the morphology [8,12], self-doping and surface modification [13–16]. Meanwhile, constructing semiconductor heterostructure is one of the effective methods to enhance the generation and separation of photoinduced electron–hole, which ultimately obtained excellent photocatalytic activity. Many BOC -based heterostructure photocatalysts such as $\text{BiOCl}/\text{Bi}_2\text{O}_3$ [17], $\text{g-C}_3\text{N}_4/\text{BiOCl}$ [18,19], WO_3/BiOCl [20], $\text{BiOCl}/\text{Bi}_2\text{S}_3$ [21] et al. were reported, and had been developed to enable the utilization of BOC in the visible-light region and improved the photocatalytic activity. According previous reports [17–21,44,45], the well matched band-structure of heterostructures played an important role in the photocatalytic activity. The similar structures of different compounds that used for constructing semiconductor heterostructure facilitated the for-

* Corresponding authors. Fax: +86 591 8377 9251.

E-mail addresses: lhx@fzu.edu.cn (H. Lin), xwang@fzu.edu.cn (X. Wang).

mation of semiconductor heterostructure and thus may exhibit higher photocatalytic activity. B_3O_4C is another layered structure Sillén related oxide. The polarizing fields existing in its local structures and the permanent static electric fields between $[Bi_3O_4]$ and $[Cl]$ layers can work as accelerators for the separations of electron hole pairs upon photo-excitation. In addition, B_3O_4C has band gap at 2.79 eV that can be excited by visible light. Huang et al. has reported the photocatalytic activity of B_3O_4C was higher than that of anatase-type TiO_2 under UV light illumination. They confirmed that Bi-based oxychloride B_3O_4C exhibited photocatalytic degradation activity of methyl orange in water under visible-light irradiation [22]. Therefore, it inspires us that the well-matched overlapping band-structure of BOC and B_3O_4C is quite suitable for constructing heterostructures and will endow BOC with efficient visible-light photocatalytic activity. But many methods for preparing semiconductor heterostructure are mostly used by multi-step synthesis, which can obtain heterostructures semiconductor but used in multi-step synthesis with raising the cost of supplies.

In the present study, B_3O_4C/BOC plate-on-plate heterojunction photocatalyst was prepared by one pot hydrothermal synthesis method. By compared with traditional method, this method was simple, convenient and easier to obtain well matched B_3O_4C/BOC heterojunction. The B_3O_4C/BOC heterojunction photocatalyst exhibited higher photocatalytic activity than the pure B_3O_4C and BOC. In addition, the B_3O_4C/BOC heterojunction photocatalyst also exhibited much higher photocatalytic activity than that of prepared by traditional two-step synthesis towards the degradation of Orange II under visible light illumination. Finally, the possible mechanisms of the enhancement of photocatalytic activity in B_3O_4C/BOC under visible-light irradiation were also discussed.

2. Experimental

2.1. Materials

All chemical reagents used in this experiment were analytical reagent grade and without further purification. Bismuth nitrate pentahydrate ($Bi(NO_3)_3 \cdot 5H_2O$), potassium chloride (KCl), sodium hydroxide (NaOH), Orange II ($C_{16}H_{11}N_2NaO_4S$) and ethanol were all obtained from Sinopharm Chemical Reagent Co. Ltd. Deionized water was used throughout the work.

2.2. Sample preparation

2.2.1. One-pot synthesis of B_3O_4C/BOC heterojunction

In a typical procedure, 4 mM of $Bi(NO_3)_3 \cdot 5H_2O$ and 4 mM of KCl were added in 70 mL deionized water at room temperature under continuous stirring, and then 1 M NaOH was added dropwise to adjust the volume value. After stirring for 0.5 h, the mixture solution was transferred into a 100 mL Teflon-lined stainless autoclave. The autoclave was heated at 120 °C for 10 h under autogenous pressure, and then cooled to room temperature naturally. The resulting product were gathered and rinsed with deionized water thoroughly, and finally dried at 60 °C. Thereby, a series of B_3O_4C/BOC photocatalysts with the different mass ratios were prepared by adjusting the concentrations of B_3O_4C . The prepared samples were denoted as xB_3O_4C/BOC , where x refers to the controlled volume ratio of NaOH ($x = 0, 0.35, 0.50, 0.60, 1$), which would also be abbreviated as BOC, 0.35 B_3O_4C/BOC -1, 0.50 B_3O_4C/BOC -1, 0.60 B_3O_4C/BOC -1, B_3O_4C . For comparison, 0.5 B_3O_4C/BOC -1 heterojunctions were also prepared from the reaction time of different stages.

2.2.2. Two-step traditional synthesis of B_3O_4C/BOC heterojunction

The synthesis of B_3O_4C/BOC composite was similar to a modified hydrothermal method [32,37]. BOC was prepared in advance.

The synthesis of BOC was fabricated via an early reported approach [16]. 4 mM of $Bi(NO_3)_3 \cdot 5H_2O$ and 4 mM of KCl were added in 70 mL deionized water at room temperature under continuous stirring. After stirring for 0.5 h, the mixture solution was transferred into a 100 mL Teflon-lined stainless autoclave. The autoclave was heated at 120 °C for 10 h under autogenous pressure, and then cooled to room temperature naturally. The resulting products were gathered and rinsed with deionized water thoroughly, and finally dried at 60 °C.

Then, the precursor of BOC was dispersed in 70 mL deionized water and stirred for 30 min. Meanwhile a moderate amount of 1 M NaOH was transferred into the solution. The mixture solution was transferred into a 100 mL Teflon-lined stainless autoclave. The autoclave was heated at 120 °C for 10 h under autogenous pressure, and then cooled to room temperature naturally, collected, washed and dried at 60 °C in air. The sample was denoted as 0.5 B_3O_4C/BOC -2.

2.3. Characterization

Crystal structure identification was performed using Bruker D8 X-ray diffractometer (XRD) with $Cu K\alpha$ radiation operating at 40 kV and 40 mA. The morphologies of B_3O_4C/BOC heterojunction photocatalysts were observed by an FEI Nova NanoSEM 230 field-emission scanning electron micro-scope (SEM). Microstructures and selected area electron diffraction (SAED) patterns were investigated using TecnaiG2 F20 S-TWIN (FEI Company) Transmission electron microscopy (TEM) with a field emission gun at 200 kV. The compositions were verified by energy dispersive X-ray analysis (EDX, equipped with TEM TecnaiG2 F20 S-TWIN). The Brunauer–Emmett–Teller (BET) specific surface areas of the samples were evaluated on the basis of nitrogen adsorption isotherms using a Micromeritics ASAP 2020 gas adsorption apparatus (USA). Diffuse reflection spectra (DRS) of the samples were recorded on a VarianCary-500 spectrophotometer, using $BaSO_4$ as the reference. UV-vis spectra were measured on a UV-vis-NIR spectrometer (Cary-500). The photoluminescence (PL) spectra were obtained using an Edinburgh Analytical Instrument FL/FSTCSPC920 Spectrophotometer. Laser Raman spectra were recorded at room temperature on a Renishaw inVia Raman system and the laser line at 532 nm was used as an excitation source. X-ray photoelectron spectroscopy (XPS) analysis was collected on a PHI Quantum 2000 Scanning ESCA Microprobe (PHYSICAL ELECTRON-ICS) with monochromatic $Al K\alpha_{1,2}$ radiation ($E = 1486.60$ eV) and CAE ($E_p = 187.85$ eV or 58.70 eV). The B_3O_4C/BOC ratio in these as-prepared samples was analyzed on an Inductively Coupled Plasma Optical Emission Spectrometry (ICP-OES) (OPTIMA 8000, PE, USA) and EA (Vario EL-Cube-Elementar). Total organic carbon (TOC) was analyzed by TOC measuring instrument (Shimadz TOC-5000). The detection of activated species was conducted by the spin-trapping electron spin resonance (ESR) measurement on a Bruker model A300 spectrometer. The settings were as follows: center field, 3512 G; microwave frequency, 9.86 GHz; microwave power, 20 mW.

2.4. Photocatalytic activity measurement

The visible light photocatalytic activity of all the samples was estimated by degradation of Orange II under visible light irradiation. In a typical photocatalytic experiment, the photocatalyst (10 mg) was dispersed in 80 mL Orange II solution (20 ppm) with a pyrex glass reactor. A 300 W Xe lamp was used with cut-off filter to provide visible light (≥ 420 nm). Prior to irradiation, stirring in dark for 30 min was allowed for establishment of adsorption/desorption equilibrium. At given irradiation time intervals, 3 mL of the solution was taken out and centrifuged and then analyzed on the UV-vis

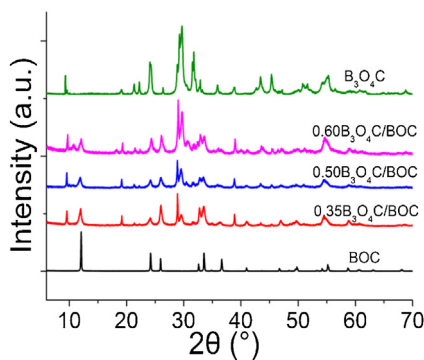


Fig. 1. XRD patterns of different samples prepared by one-pot method.

spectrometer. The final decoloration efficiency (DE) was calculated by the following equation:

$$\text{DE}_t (\%) = \frac{C_t}{C_0} \times 100\%, \quad (1)$$

where C_t and C_0 stand for the concentration of reactants at a certain irradiation time t and at initial, respectively.

2.5. Photoelectrochemical measurement

Photoelectrochemical characterization was conducted on a ZENNIMUM electrochemical workstation (Zahner, Germany) with a standard three-electrode system. The prepared samples served as the working electrode with an active area of ca. 0.25 cm^2 . The counter and reference electrodes were Pt plate and Ag/AgCl electrode and 0.2 M Na₂SO₄ (pH 6.8) was used as electrolyte. A 300 W xenon lamp was used to provide UV light.

3. Results and discussion

3.1. Morphology and structure

3.1.1. XRD and Raman analyses

XRD analysis was carried out to investigate the phase structures of the catalysts. Fig. 1 shows the X-ray diffraction (XRD) patterns of the samples obtained by one-pot method. It could be found that the pure BOC showed the diffraction peaks of (0 0 1), (0 0 2), (1 0 1), (1 0 1), (1 1 0), (1 0 2), (2 1 1), (1 0 4) planes with $2\theta = 11.98^\circ$, 24.10° , 25.86° , 32.50° , 33.45° , 54.10° and 55.11° , which can be well indexed to tetragonal phase BOC (JCPDS No. 06-082-0249) [23]. As for the pure B₃O₄C, the diffraction peaks with $2\theta = 9.31^\circ$, 19.09° , 21.28° , 23.98° , 28.78° , 29.13° and 29.68° corresponded to the (2 0 0), (4 0 0), (3 1 0), (2 1 -1), (6 0 0), (4 1 -1) and (4 1 1) planes in the monoclinic phase of Bi₃O₄Cl (JCPDS No. 36-0760) [24]. The XRD analysis indicated the co-existence of BOC and B₃O₄C phases in the as-prepared B₃O₄C/BOC nanocomposite and no other new phases were observed in the XRD patterns. With mass ratio of B₃O₄C in the composites increasing, the peak intensities of the B₃O₄C increased, whereas those of the BOC lowered gradually. Fig. S1 shows the XRD patterns of the 0.50B₃O₄C/BOC-1 samples prepared by varied hydrothermal reaction of 5 h, 10 h and 24 h. With the time of reaction prolonging, the peak intensities of the heterojunction increased and then the samples had reached a perfect degree of crystal after 10 h.

Apart from XRD, Raman measurements were carried out. Fig. S5 shows the Raman spectra of pure BOC, 0.50B₃O₄C/BOC and pure B₃O₄C samples. The BiOX with a space group of D_{4h}⁷, has two molecular formulas per unit cell with the Raman active modes of A_{1g}, B_{1g}, and E_g. Pure BOC shows two intense bands centered at some 60 cm^{-1} and 145 cm^{-1} that are assigned to the A_{1g} external

and internal Bi–Cl stretching mode, respectively. The band located at 199 cm^{-1} can be attributed to the E_g internal Bi–Cl stretching mode, while E_g external Bi–Cl one is probably masked by the strongest band at 145 cm^{-1} [16]. E_g and B_{1g} band, produced by motion of the oxygen atoms, at about 396 cm^{-1} is very weak and is not easy to observe [20]. While the wavenumber of pure B₃O₄C here is smaller and more decentralized than the bulk BOC (A_{1g} 60 – 145 cm^{-1} , E_g 199 cm^{-1}), which may be attributed to the stronger orientation of plate-like single crystal structure [38] and became weak of Bi–Cl band. E_g and B_{1g} band, produced by motion of the oxygen atoms, at about 320 cm^{-1} and 440 cm^{-1} are very strong. After coupling the two components, most of the bands for BOC and B₃O₄C die down or vanished and only the band of BOC at 144 cm^{-1} with a relatively strong intensity was preserved. A new broadened band at 390 cm^{-1} and 639 cm^{-1} appeared. The reduction of original bands of BOC and B₃O₄C and the generation of new band further confirmed the construction of heterojunction.

3.1.2. SEM, TEM, EDX, BET and ICP analyses

The morphology and microstructure of the hierarchical B₃O₄C/BOC composites were observed by SEM, TEM, HRTEM and EDX images. SEM images of different samples were shown in Fig. 2. The morphology of the pure BOC sample was a sheet-shaped structure with a micrometer-scale width and an average thickness of 50–150 nm (Fig. 2a). On the contrary, B₃O₄C demonstrated a nanoslices feature with even thinner thickness than BOC (Fig. 2e). Moreover, BOC/B₃O₄C nanoplates had no obvious stacking or aggregation, and the surfaces of BOC nanoplates were well covered by two-dimensional B₃O₄C nanoslices. For the B₃O₄C/BOC composites, an irregular multi-plate structure with morphology ranging from flower-like to plates can be observed due to the controlled volume ratio of NaOH, which indicated the plate-on-plate structure is possibly formed by self-assembly of B₃O₄C and BOC nanoplates (Fig. 2b–d). Taking this one step further, it indicated that B₃O₄C nanoslices were gradually grown on BOC nanoplates during the hydrothermal reaction via the crystallization, dissolution and recrystallization process that were similar to previous reports [25,26]. To better understand the formation mechanism, the B₃O₄C/BOC-1 composites synthesized at different reaction times were characterized by SEM and the images are shown in Fig. S2. At the initial reaction stage (5 h), it could be found that a thin flower-like layer of B₃O₄C slices grow uniformly on the surfaces of 2D plat and form structure of BOC nanoplates. As reaction time extended to 10 h, these small crystallites gradually aggregated into large nanoplates with higher crystallinity. After a reaction time of 24 h, the B₃O₄C/BOC became high even larger thickness (Fig. S2c) but the crystallinity of 0.50B₃O₄C/BOC-1 was almost same to the sample of 10 h (Fig. 1). Nanosheets with thinner thickness demonstrated a relatively high activity, which was probably ascribed to its low electron injection barrier and high electron mobility on the sheet surface [27]. Thus, we hold opinion that the sample of 10 h might exhibit excellent shape-dependent visible-light-driven photocatalytic activities.

More structural information of 0.50B₃O₄C/BOC samples that prepared by two different ways were provided by TEM analysis. The TEM image in Fig. 3a reveals that the 0.50B₃O₄C/BOC-1 was a irregular platelet shaped nanostructure with thickness ranging from 200 nm to 1 um, which was consistent with the SEM observations in Fig. 2. The teethlike nanosheets structure proved that the B₃O₄C nanoslices were well dispersed on the surfaces of BOC nanoplates. The resolved lattice fringes of 0.275 nm and 0.401 nm shown in Fig. 3b were coincided with the fringe spacing of the (1 1 0) lattice plane of the tetragonal BOC sheet and the (0 4 0) crystal plane of the monoclinic B₃O₄C, respectively, which revealed the high crystallinity of B₃O₄C and BOC. The angle indicated by the corresponding SAED results (Fig. 3b, inset) was 90° , which was identical

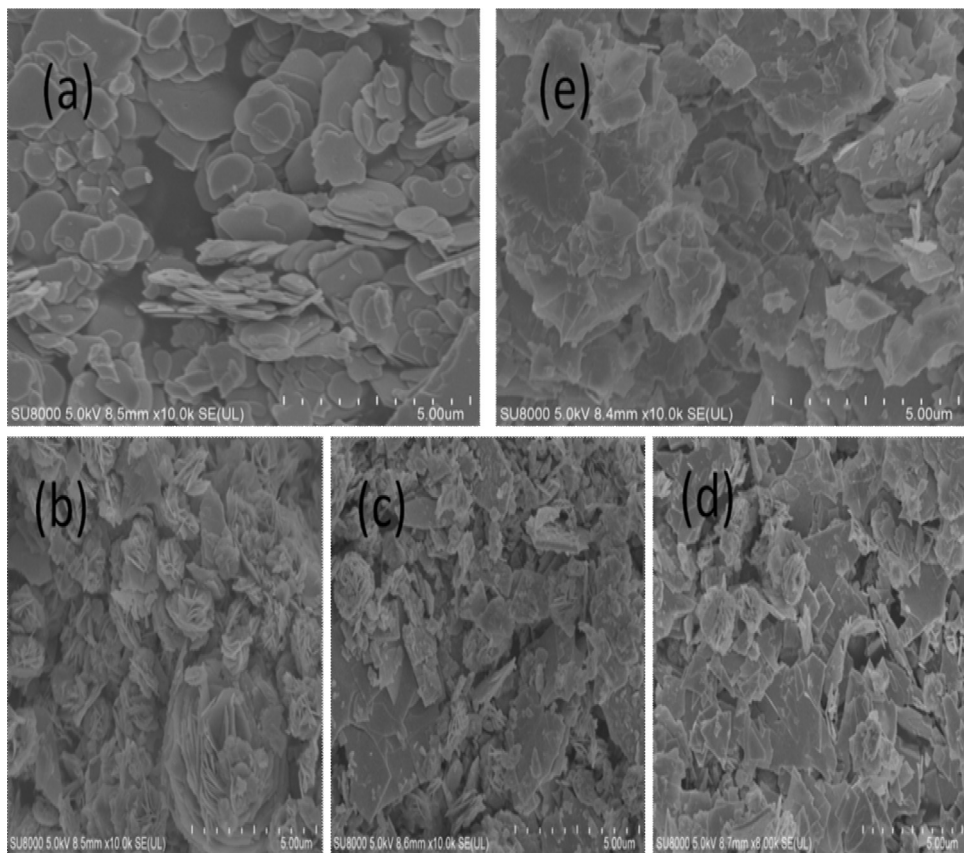


Fig. 2. SEM images of different samples: (a) BOC, (b) 0.35B₃O₄C/BOC-1, (c) 0.50B₃O₄C/BOC-1, (d) 0.60B₃O₄C/BOC-1, (e) B₃O₄C.

to the theoretical value of the angle BOC (110) and B₃O₄C (011) faces. According to the symmetry of tetragonal BOC and monoclinic B₃O₄C, the largely exposed plane can be identified as {001} facets. In addition, the EDX spectrum shown in Fig. 3c reveals that the elements on the surface of B₃O₄C/BOC mainly concluded the O, Bi and Cl, and the content of B₃O₄C were about 50%. Meanwhile, the total elemental compositions of metal for 0.50BOC/B₃O₄C were determined by ICP-OES, and the content of oxygen were measured by EA. As shown in Table S2, the surface metal content of Bi for 0.50BOC/B₃O₄C-1 is 82.10% and the Bi content for 0.50BOC/B₃O₄C-2 is 90.41% that are similar to theoretical calculation (84.71%). The content of O for 0.50BOC/B₃O₄C-1 is 8.23% and the total content O for 0.50BOC/B₃O₄C-2 (7.66%). According to these results, the Bi to O atom ratios for 0.50BOC/B₃O₄C-1 and 0.50BOC/B₃O₄C-2 are 3.9/5.1 and 4.3/4.7, respectively. As shown, the Bi/O (4/5) ratio of 0.50BOC/B₃O₄C by theoretical calculation is identical to that of 0.50BOC/B₃O₄C-1. This further confirmed the specific ratio was close to 1/1 between BOC and B₃O₄C in 0.50BOC/B₃O₄C. These facts demonstrated that B₃O₄C/BOC heterostructures were successfully fabricated. As for 0.50B₃O₄C/BOC-2 that prepared by two-step traditional method, the highresolution TEM (HRTEM) images and EDX spectrum in Fig. 3e and f reveals that the structure and the content of B₃O₄C of the B₃O₄C/BOC-2 were almost identical to that of 0.50B₃O₄C/BOC-1, which supposed that the BOC and B₃O₄C had also well mixed heterojunctions by two-step traditional method. However, the 0.50B₃O₄C/BOC-2 nanosheets were obvious thicker than that of 0.50B₃O₄C/BOC-1 as shown in Fig. 3a and d. The different synthesis methods not only affect the thickness of nanosheets but also have some effects on other physical and chemistry properties [5,8,12]. In this work, the surface areas and photocatalytic properties of the two samples were compared. As can be seen in Table 1, the surface area of 0.50B₃O₄C/BOC-1 was about 10 m²/g,

Table 1
Specific BET surface areas parameters of the as-prepared B₃O₄C/BOC samples.

Catalyst code	BET surface area ^a (m ² /g)
BOC	1.7400
B ₃ O ₄ C	1.6768
0.50B ₃ O ₄ C/BOC-1	9.0948
0.50B ₃ O ₄ C/BOC-2	6.9811

^a Calculated by the Brunauer–Emmett–Teller (BET) method.

which was obvious higher than that of 0.50B₃O₄C/BOC-2. In addition, the surface area of 0.50B₃O₄C/BOC was significantly larger than that of pure BOC and B₃O₄C, indicating that the amount of added B₃O₄C might have highly influence on the textural properties of the coupled samples.

3.2. DRS and XPS analysis

The optical absorption properties of the as-prepared samples investigated by UV-vis spectrophotometer were shown in Fig. 4. We observed that the pure BOC showed an absorption edge around 360 nm and the pure B₃O₄C sample showed an absorption edge around 450 nm. When compared with pure BOC, the B₃O₄C/BOC demonstrated light absorption in the visible light region. Furthermore, with the mass ratio of B₃O₄C to BOC increased from 0.35 to 0.60, the absorption edge of B₃O₄C/BOC increased from 410 to 440 nm. Fig.S3 plotted the integrated intensity of the band at 350 nm versus the mass ratio of B₃O₄C to BOC. This good linear relation indicated that the enhanced visible light absorption of B₃O₄C/BOC might be mainly due to B₃O₄C.

Based on their absorption spectra, the band gap energy (E_g) of a semiconductor can be calculated from the following equation [22,28]: $\alpha h\nu = A(h\nu - E_g)^{n/2}$ where α , h , ν , A and E_g are the absorp-

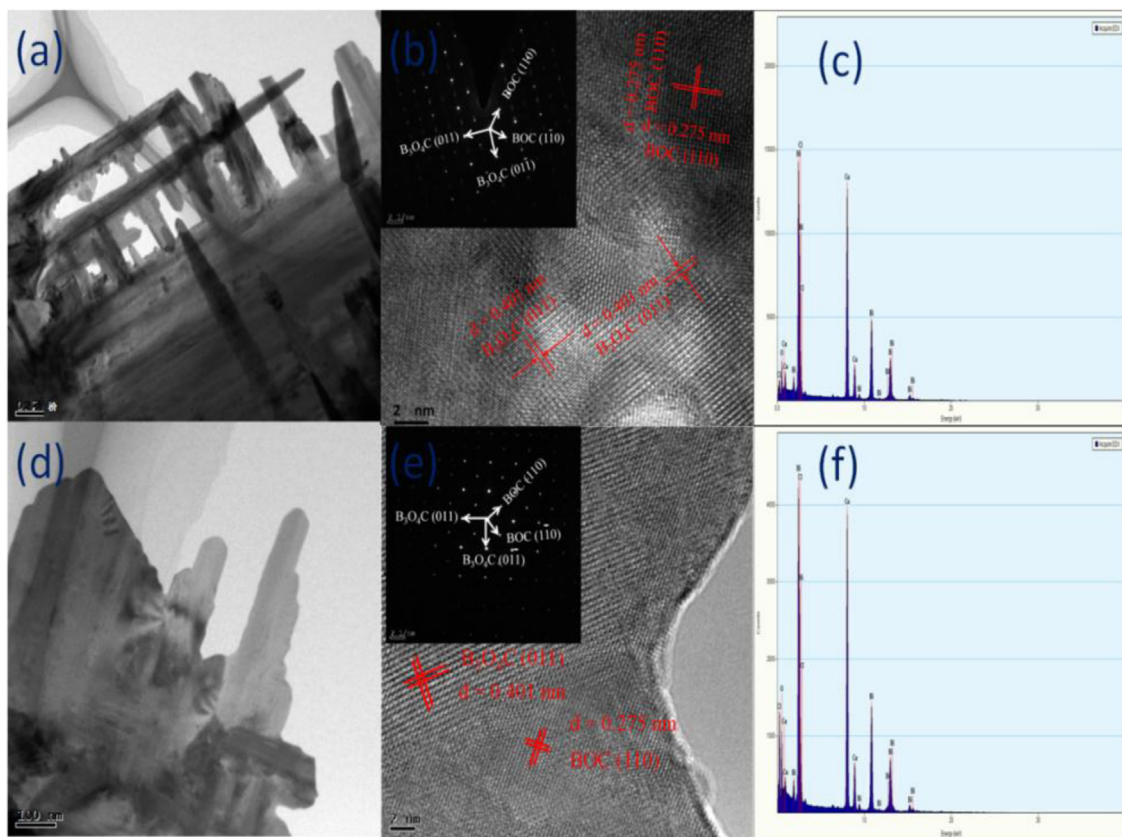


Fig. 3. TEM analyses of two $0.50\text{B}_3\text{O}_4\text{C}/\text{BOC}$ samples prepared by different ways: (a) TEM image of sample $0.50\text{B}_3\text{O}_4\text{C}/\text{BOC-1}$; (b) HRTEM image of sample $0.50\text{B}_3\text{O}_4\text{C}/\text{BOC-1}$, the inset image is the SAED patterns; (c) EDX spectrum of $0.50\text{B}_3\text{O}_4\text{C}/\text{BOC-1}$ sample; (d) TEM image of sample $0.50\text{B}_3\text{O}_4\text{C}/\text{BOC-2}$; (e) HRTEM image of sample $0.50\text{B}_3\text{O}_4\text{C}/\text{BOC-2}$, the inset image is the SAED patterns; (f) EDX spectrum of $0.50\text{B}_3\text{O}_4\text{C}/\text{BOC-2}$ sample.

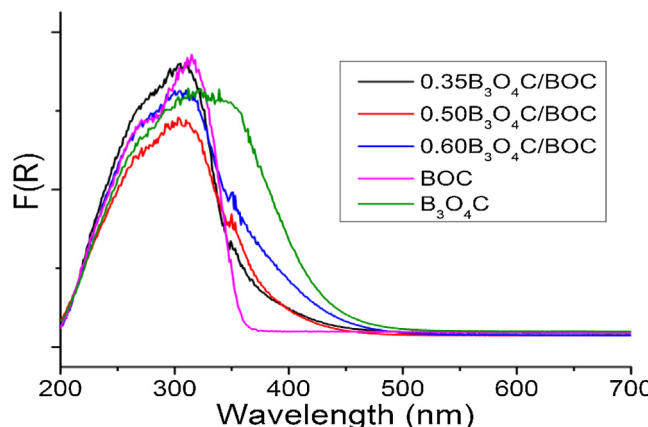


Fig. 4. DRS spectra of heterojunction samples with varied composition ratios obtained by one-pot synthesis.

tion coefficient, Planck constant, light frequency, proportionality constant and band gap, respectively. According to this, the E_g of BOC ($\lambda = 360 \text{ nm}$) and $\text{B}_3\text{O}_4\text{C}$ ($\lambda = 450 \text{ nm}$) was determined from the formula $\lambda_g = 1239.8/E_g$ and obtained to be 3.44 eV and 2.76 eV. Moreover, the E_g of $\text{B}_3\text{O}_4\text{C}/\text{BOC}$ composites was located from 3.0 to 2.82 eV. These results indicated that the $\text{B}_3\text{O}_4\text{C}/\text{BOC}$ heterostructure semiconductor with a matching energy band position had formed and may be suitable for the photocatalytic decomposition of organic contaminants under visible-light irradiation.

The chemical states of the BOC, $\text{B}_3\text{O}_4\text{C}$ and $0.50\text{B}_3\text{O}_4\text{C}/\text{BOC}$ composite photocatalysts were investigated by XPS analysis. As shown in Fig. 5a, only C, Bi, O and Cl were detected in the sample. The C1s

peak at around 284.6 eV can be attributed to the signal from carbon contained in the instrument and was used for calibration [37]. Fig. 5b shows the $\text{Bi} 4f_{5/2}$ and $\text{Bi} 4f_{7/2}$ XPS core lines with B.E. locating around 164.74 eV and 159.38 eV or 163.51 eV and 158.40 eV, which are assigned to Bi^{3+} in BOC or $\text{B}_3\text{O}_4\text{C}$ [13]. An additional spin-orbit doublet with binding energy of 156.91 and 157.00 eV for $\text{Bi} 4f_{7/2}$ was also observed in $0.50\text{B}_3\text{O}_4\text{C}/\text{BOC-1}$ and $0.50\text{B}_3\text{O}_4\text{C}/\text{BOC-2}$ samples, suggesting that certain parts of bismuth existed in the $\text{Bi}^{(3-x)+}$ valence state. It indicated that the Bi^{3+} partially reduced to the lower valence state by the hydrothermal composites synthesized method. A similar chemical shift of approximately 2.2–2.6 eV for $\text{Bi} 4f_{7/2}$ was also observed by Sato et al [30], and Chen et al [26,39]. They concluded that $\text{Bi}^{(3-x)+}$ formal oxidation state could probably attribute to the substoichiometric forms of Bi within the $[\text{Bi}_2\text{O}_2]$ layer, and the formation of the low oxidation state contributed to oxygen vacancy in the crystal lattice. There are two different oxygen species presented on the surface of the series samples (Fig. 5c). The O1s B.E. around 532.04–532.38 eV is due to the $\text{Bi}-\text{O}$ bond in all samples, and the O1s peak at 529.94–530.50 eV due to the surface hydroxyl groups ($\text{Bi}-\text{O}-\text{H}$) on the samples [13,26]. From Fig. 5d, the binding energy of 198.21–198.34 eV and 199.73–199.87 eV was referred to the $\text{Cl} 2p_{3/2}$ and $2p_{1/2}$ respectively which could be assigned to Cl at the monovalent oxidation state, suggesting that the $\text{B}_3\text{O}_4\text{C}/\text{BOC}$ heterostructure did not affect the inter-layered Cl^- [37].

3.3. Photocatalytic activity

The photocatalytic activities of BOC, $\text{B}_3\text{O}_4\text{C}$ and $0.50\text{B}_3\text{O}_4\text{C}/\text{BOC-1}$ were examined by photocatalytic degradation of Orange II upon visible-light irradiation as shown in Fig. 6. The Orange II molecule

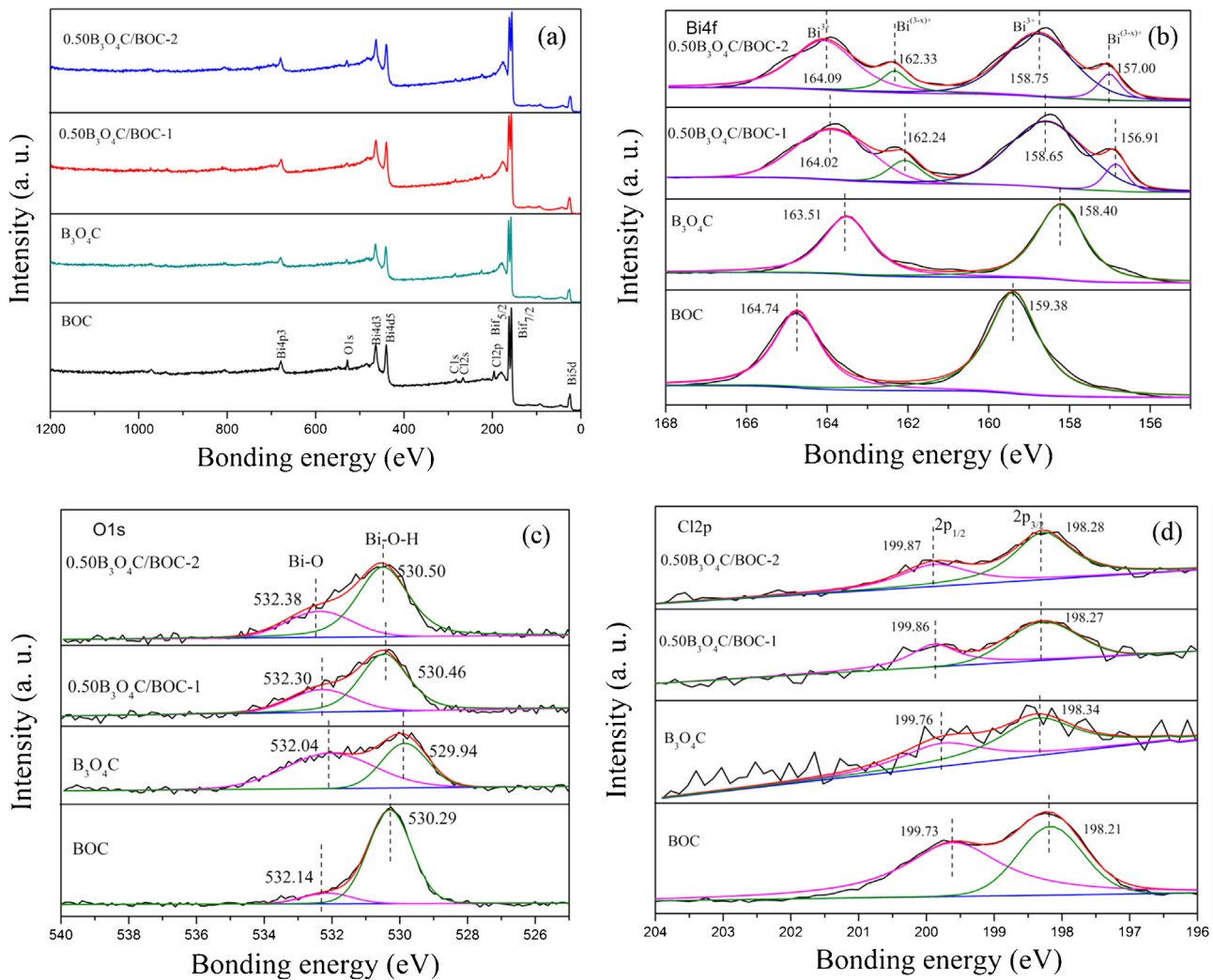


Fig. 5. High resolution XPS spectra of pure BOC, pure B_3O_4C and 0.50 B_3O_4C/BOC . (a) Total survey; (b) Bi 4f; (c) O 1s; (d) Cl 2p.

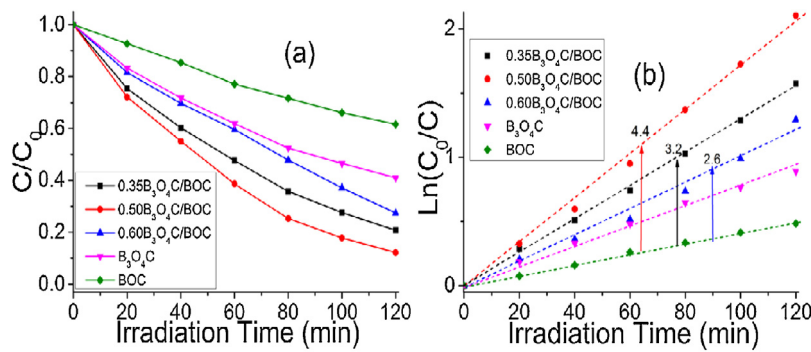


Fig. 6. One-pot synthesis of samples: time course of the decrease in the concentration (a) and $\ln(C_0/C)$ (b) for the photodegradation of orange II under visible irradiation.

is quite stable under visible light illumination and is difficult to be photodegraded in the absence of photocatalyst [16,29]. As can be seen from Fig. 6a, the photocatalytic degradation efficiency of Orange II was 25.0%, 53.5%, 78.0%, 92.0% and 70.0% for the pure BOC, pure B_3O_4C , 0.35 B_3O_4C/BOC , 0.50 B_3O_4C/BOC and 0.60 B_3O_4C/BOC after irradiation for 120 min, respectively. The DE_t of Orange II over pure BOC is only 25.0%, indicating that the activity of BOC with regard to Orange II degradation is poor and that any dye photosensitization can be neglected. However, the B_3O_4C/BOC composites showed a sharp increase in Orange II degradation when compared

with pure BOC and pure B_3O_4C , in which the 0.50 B_3O_4C/BOC -1 exhibited the best photocatalytic degradation efficiency.

It has been reported that some degradation intermediates are more carcinogenic and toxic than the parent dyes [40,41]. Prior to wastewater discharge, dye components are completely mineralized by photocatalysts which is highly desirable. Nevertheless, it is not easy to achieve a high mineralization rate during the visible-light photocatalytic degradation. Thus, the kinetics of total organic carbon (TOC) disappearance was examined after photocatalytic tests. Fig. S6 shows TOC removal of Orange II of pure

Table 2

One-pot synthesis of different samples: degradation rate constants (k_a) and relative coefficients (R^2) in decomposing Orange II.

Catalyst code	$k_a(\text{min}^{-1})$	R^2	$k_a/A(\text{g m}^{-2} \text{ min}^{-1})$
BOC	4.00×10^{-3}	0.993	2.30×10^{-3}
$\text{B}_3\text{O}_4\text{C}$	7.00×10^{-3}	0.990	4.17×10^{-3}
$0.35\text{B}_3\text{O}_4\text{C}/\text{BOC}$	1.28×10^{-2}	0.992	1.70×10^{-3}
$0.50\text{B}_3\text{O}_4\text{C}/\text{BOC}$	1.76×10^{-2}	0.989	1.96×10^{-3}
$0.60\text{B}_3\text{O}_4\text{C}/\text{BOC}$	1.04×10^{-2}	0.983	1.46×10^{-3}

Note: A_{BET} surface area.

BiOCl , pure $\text{Bi}_3\text{O}_4\text{Cl}$ and $0.50\text{Bi}_3\text{O}_4\text{Cl}/\text{BiOCl}-1$, $0.50\text{Bi}_3\text{O}_4\text{Cl}/\text{BiOCl}-2$ with increasing irradiation time. The $0.50\text{B}_3\text{O}_4\text{C}/\text{BOC}$ exhibits the much higher TOC removal rate than pure BiOCl and pure $\text{Bi}_3\text{O}_4\text{Cl}$, in which the $0.50\text{Bi}_3\text{O}_4\text{Cl}/\text{BiOCl}-1$ exhibits the highest mineralization rate. The mineralization rate are decreased in the order of $0.50\text{B}_3\text{O}_4\text{C}/\text{BOC}-1 > 0.50\text{B}_3\text{O}_4\text{C}/\text{BOC}-2 > \text{pure BOC} > \text{pure B}_3\text{O}_4\text{C}$, indicating that the Orange II was not only decolorized but also mineralized by $0.50\text{B}_3\text{O}_4\text{C}/\text{BOC}$.

The degradation kinetics of Orange II using $\text{B}_3\text{O}_4\text{C}$, BOC and $\text{B}_3\text{O}_4\text{C}/\text{BOC}$ photocatalysts were investigated by fitting the experimental data to the Langmuir–Hinshelwood model (Eq. (2)):

$$r = \frac{-dc}{dt} = \frac{k_r KC}{(1 + KC)} \quad (2)$$

Because the reactant concentration was low (the term $KC \rightarrow 0$), the Eq. (2) was reduced to the pseudo first-order kinetics equation (Eq. (3)) [30]:

$$\frac{\ln C}{C_0} = k_a t \quad (3)$$

where C is the concentration of Orange II remaining in solution after irradiation, C_0 is the initial concentration of Orange II before irradiation and k_a is the apparent rate constant (min^{-1}). The variations in $\ln(C_0/C)$ as a function of illumination time were given in Fig. 6b. The pseudo-first-order constants (k_a) and relative coefficients (R^2) were summarized in Table 2. It is found that the $0.50\text{B}_3\text{O}_4\text{C}/\text{BOC}$ heterostructures exhibit the highest degradation rate. The rate constant of $0.50\text{B}_3\text{O}_4\text{C}/\text{BOC}$ is 0.0176 min^{-1} , which is about 2.5-fold as high as that of $\text{B}_3\text{O}_4\text{C}$ ($k_a = 0.007 \text{ min}^{-1}$) and 4.4-fold as high as that of BOC ($k_a = 0.004 \text{ min}^{-1}$). The rate constants of $0.35\text{B}_3\text{O}_4\text{C}/\text{BOC}$ and $0.60\text{B}_3\text{O}_4\text{C}/\text{BOC}$ are lower than that of $0.50\text{B}_3\text{O}_4\text{C}/\text{BOC}$ but higher than pure $\text{B}_3\text{O}_4\text{C}$ and BOC. These results suggested that constructing heterostructure of BOC with $\text{B}_3\text{O}_4\text{C}$ nanoslices was efficient to enhance the visible light photocatalytic activity. In addition, there was optimal mass ratio of BOC to $\text{B}_3\text{O}_4\text{C}$ that exhibits the best photocatalytic activity. It is well-known that many factors, such as surface structure, chemistry composition and synthesis methods, et al. have great effects on the photocatalytic activity [31]. In this case, on one hand, the difference of thickness from BOC to $\text{B}_3\text{O}_4\text{C}$ (Fig. 2) was seem to not enough to explain the activity difference between them. On the other hand, although pure $\text{B}_3\text{O}_4\text{C}$ exhibited the strongest visible absorption among the above samples, it did not exhibit the best photocatalytic activity probably due to the rapid recombination of charge carrier. What's more, to understand the surface activities of the $\text{B}_3\text{O}_4\text{C}/\text{BOC}$ composites, we normalized the apparent rate constants with specific surface areas of the photocatalysts. As shown in Table 2, it seems that surface area is not a major factor in this case. Therefore, we suggested that there were synergy effect of heterostructure between $\text{B}_3\text{O}_4\text{C}$ and BOC that may benefit the enhancement of photocatalytic activity. As for heterostructure semiconductor, the well-matched overlapping band-structure may form internal electric-field at the interface and in the semiconductors, which may prompt the separation of electron–hole pairs [32]. Generally, the transient photocurrent responses have been demonstrated to be a useful technique to investigate the separa-

tion of photogenerated electron–hole pairs owing to the intrinsic band-gap structure of semiconductors [33,34]. Fig. 7 shows a comparison of the photocurrent-time (I-t) curves for the BOC, $\text{B}_3\text{O}_4\text{C}$ and $0.50\text{B}_3\text{O}_4\text{C}/\text{BOC}-1$. At the beginning, the photocurrent did not reach equilibrium. After about 60 s, the current value became stable and decreased to zero as the incident light was turned off and returned to the original value only when the light was turned on again. It can be seen the photocurrent value of $0.50\text{B}_3\text{O}_4\text{C}/\text{BOC}-1$ is higher about 67% than pure $\text{B}_3\text{O}_4\text{C}$ and about 25% than pure BOC, indicating charge separation in the photoelectron chemical process has been promoted, which may result in its highest photocatalytic activity. Meanwhile, the photocurrent value $0.50\text{B}_3\text{O}_4\text{C}/\text{BOC}-1$ is higher about 15% than $0.50\text{B}_3\text{O}_4\text{C}/\text{BOC}-2$, which implicated one-pot hydrothermal method was more beneficial to the separation of photogenerated electron–hole pairs.

To further characterize the synergy effect of heterostructure of $\text{B}_3\text{O}_4\text{C}/\text{BOC}$, the visible light activity of $0.50\text{B}_3\text{O}_4\text{C}/\text{BOC}$ samples prepared by two different ways were also compared. As shown in (Fig. S4 and Table S1), the photocatalytic degradation efficiency of Orange II of $0.50\text{B}_3\text{O}_4\text{C}/\text{BOC}-1$ is much higher than that of $0.50\text{B}_3\text{O}_4\text{C}/\text{BOC}-2$. The rate constant ($k_a = 0.0176 \text{ min}^{-1}$) of the $0.50\text{B}_3\text{O}_4\text{C}/\text{BOC}-1$ is up to 2.6-fold faster than that of $0.50\text{B}_3\text{O}_4\text{C}/\text{BOC}-2$ ($k_a = 0.00675 \text{ min}^{-1}$), indicating that the difference resulted from synthesis methods also has great effect on their photocatalytic activity. As shown in above, the $0.50\text{B}_3\text{O}_4\text{C}/\text{BOC}-1$ exhibited thinner thickness, higher surface area and higher intensity in visible light adsorption, which may benefit its separation efficiency of charge carrier under visible light illumination. To confirm this suggestion, the fluorescence emission spectra of pure BOC, pure $\text{B}_3\text{O}_4\text{C}$, $\text{B}_3\text{O}_4\text{C}/\text{BOC}-1$ and $\text{B}_3\text{O}_4\text{C}/\text{BOC}-2$ were obtained respectively using an ultraviolet light with a 312 nm wavelength as the excitation source (Fig. 8). In general, a decrease in the recombination rate gave rise to a low PL intensity [35,36]. Compared with the pure BOC, pure $\text{B}_3\text{O}_4\text{C}$ and $\text{B}_3\text{O}_4\text{C}/\text{BOC}-2$, the emission peak intensity of the $\text{B}_3\text{O}_4\text{C}/\text{BOC}-1$ decreased greatly, which suggested that the $\text{B}_3\text{O}_4\text{C}/\text{BOC}-1$ has a lower recombination rate of photo-generated charge carriers. Furthermore, the $\text{B}_3\text{O}_4\text{C}/\text{BOC}-1$ heterojunction exhibited a higher transient photocurrent density (about $0.24\text{--}0.32 \mu\text{A}/\text{cm}^2$) than that of the $\text{B}_3\text{O}_4\text{C}$, BOC and $\text{B}_3\text{O}_4\text{C}/\text{BOC}-2$ samples (Fig. 7), which indicated that the separation efficiency of photogenerated electrons and holes was significantly improved at their interface.

3.4. The possible photocatalytic mechanism of $\text{B}_3\text{O}_4\text{C}/\text{BOC}$

As discussed above, pure BOC had negligible activity for Orange II degradation under visible light irradiation but the heterojunction structure $\text{B}_3\text{O}_4\text{C}/\text{BOC}$ exhibited enhanced photocatalytic activity under visible irradiation. The reason should be closely attributed to the interaction between $\text{B}_3\text{O}_4\text{C}$ and BOC, which increased the mobility of photogenerated carriers in the photocatalyst and thus produce more active radicals during the photocatalytic reaction. To identify the reactive oxygen radicals produced from pure BOC, $0.50\text{B}_3\text{O}_4\text{C}/\text{BOC}-1$, $0.50\text{B}_3\text{O}_4\text{C}/\text{BOC}-2$ and pure $\text{B}_3\text{O}_4\text{C}$, the ESR technique with DMPO as a spin-trapping reagent was applied to obtain information on the active radicals. The superoxide radicals ($\cdot\text{O}_2^-$) and hydroxyl radicals ($\cdot\text{OH}$) are separately detected in methanol-medium and water-medium solutions [42]. As indicated in Fig. 9a, four apparent signals (1:2:2:1) were generated, which were attributed to $\cdot\text{OH}$ in $\text{B}_3\text{O}_4\text{C}$, $0.50\text{B}_3\text{O}_4\text{C}/\text{BOC}-1$ or $0.50\text{B}_3\text{O}_4\text{C}/\text{BOC}-2$ under visible light irradiation for 5 min, while no $\cdot\text{OH}$ signal was detected in dark under identical conditions. Furthermore, these $\cdot\text{OH}$ radical signals for $0.50\text{B}_3\text{O}_4\text{C}/\text{BOC}$ are much stronger than those for $\text{B}_3\text{O}_4\text{C}$ and signals for $0.50\text{B}_3\text{O}_4\text{C}/\text{BOC}-1$ are also rather stronger than $0.50\text{B}_3\text{O}_4\text{C}/\text{BOC}-2$, which are accounting for a higher photocatalytic performance of $\text{B}_3\text{O}_4\text{C}/\text{BOC}$ than

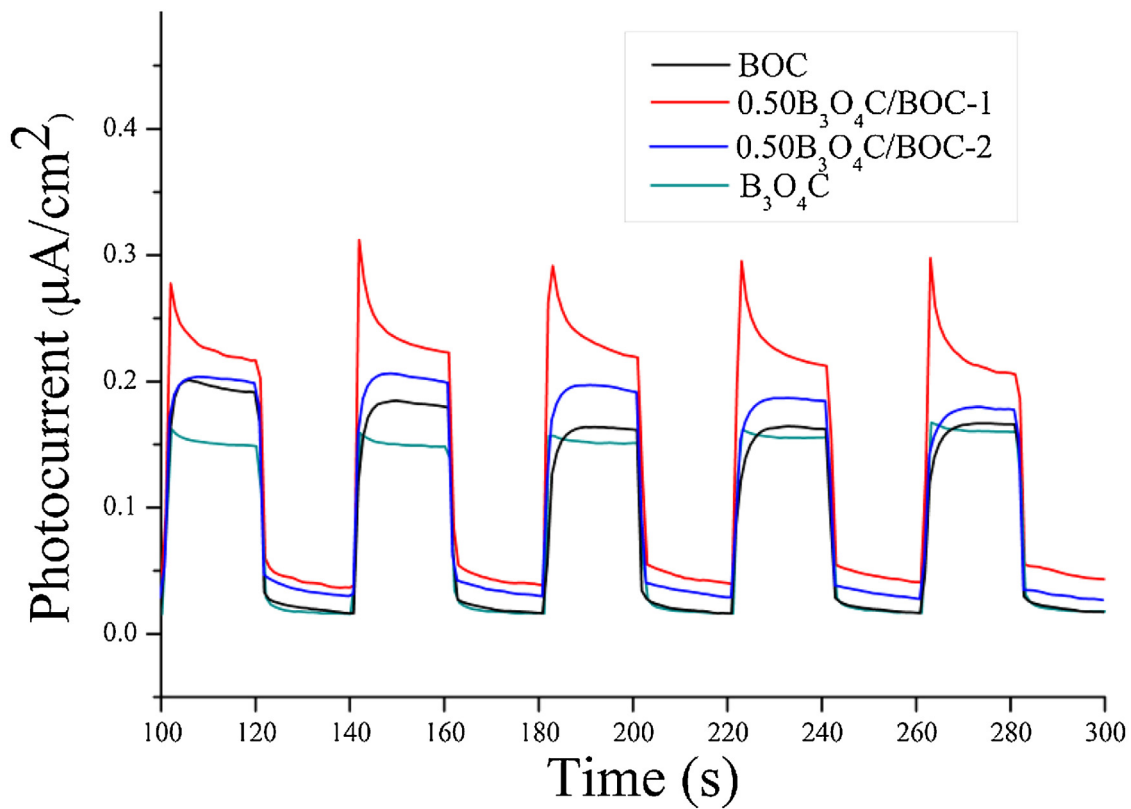


Fig. 7. Comparison of transient photocurrent response of different samples: BOC, $\text{B}_3\text{O}_4\text{C}$, $0.50\text{B}_3\text{O}_4\text{C}/\text{BOC-1}$ and $0.50\text{B}_3\text{O}_4\text{C}/\text{BOC-2}$.

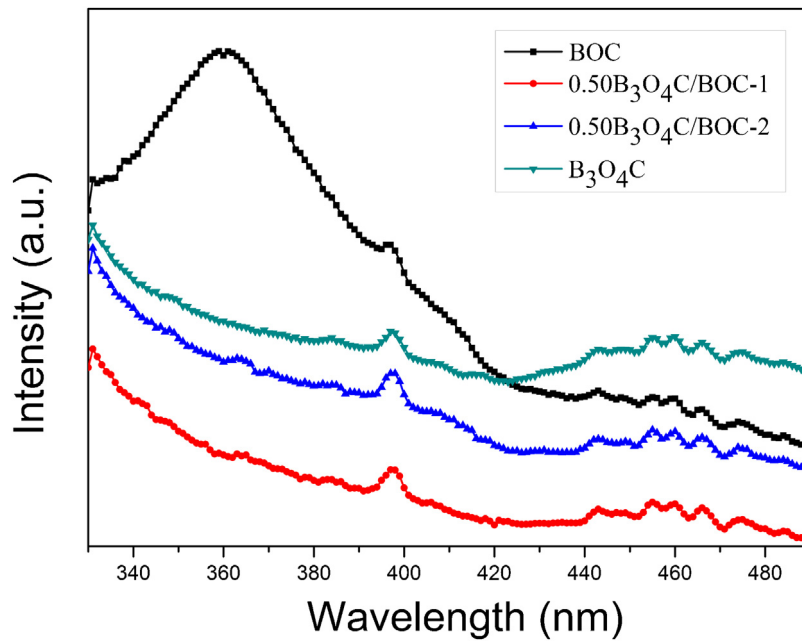


Fig. 8. Fluorescence spectra of samples: one-pot synthesis of $0.50\text{B}_3\text{O}_4\text{C}/\text{BOC-1}$, two-step synthesis of $0.50\text{B}_3\text{O}_4\text{C}/\text{BOC-2}$, $\text{B}_3\text{O}_4\text{C}$ and BOC.

BOC toward the degradation of pollutants. There are three impure peaks which are from degenerative DMPO in visible light [43]. Fig. 9b shows that the characteristic peaks (1:1:1:1) of $\bullet\text{O}_2^-$ can be detected in the methanol dispersion of $0.50\text{B}_3\text{O}_4\text{C}/\text{BOC-1}$ and $0.50\text{B}_3\text{O}_4\text{C}/\text{BOC-2}$ under visible light irradiation, which reveals that the $\bullet\text{O}_2^-$ can be produced and plays an important role in the photo-catalysis process, and the intensity of $0.50\text{B}_3\text{O}_4\text{C}/\text{BOC-1}$ is stronger to $0.50\text{B}_3\text{O}_4\text{C}/\text{BOC-2}$. These observations clearly disclose that the

strong oxidizing $\bullet\text{OH}$ and $\bullet\text{O}_2^-$ are both the active radicals and play crucial roles toward the degradation of Orange II.

Based on the above discussion, a possible mechanism of the $\text{B}_3\text{O}_4\text{C}/\text{BOC}$ heterojunction composite was proposed, as shown in Fig. 10. It has been reported that the band edge potentials of the conduction band(CB) and the valence band(VB) for BOC are -1.1 and $+2.4\text{ eV}$ [17], while those for $\text{B}_3\text{O}_4\text{C}$ are $+0.19$ and $+2.97\text{ eV}$ [24], respectively. According to the valence band (VB) spectra in Fig. S7,

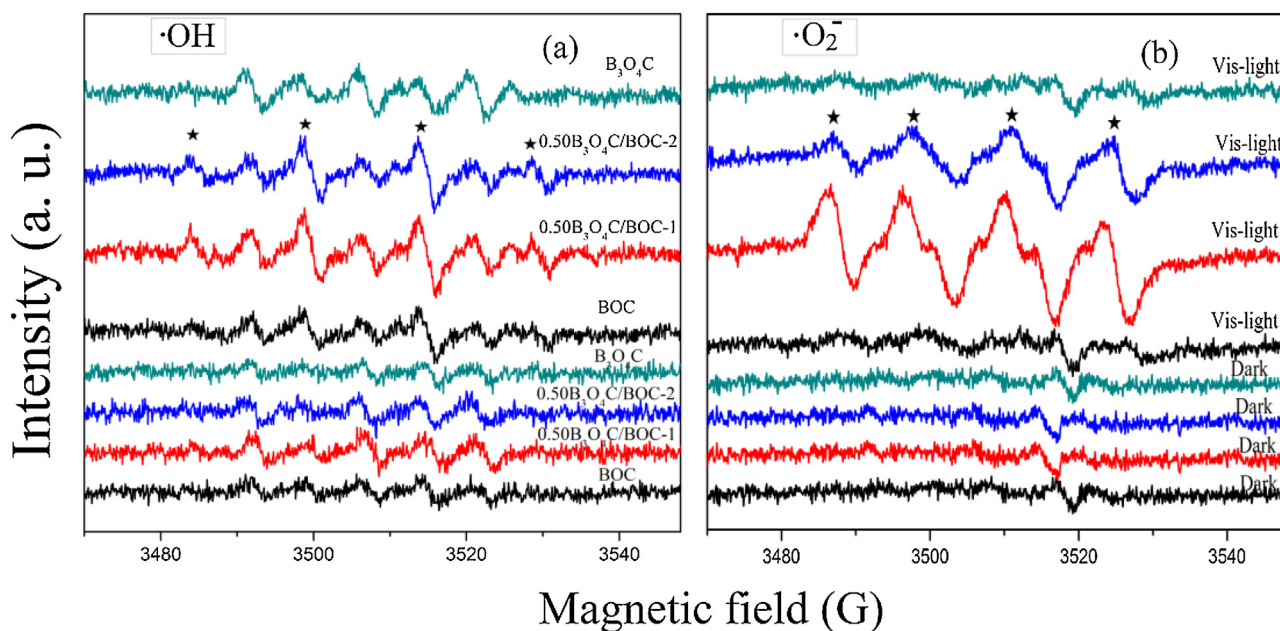


Fig. 9. DMPO spin-trapping ESR spectra recorded with BOC, $B_3O_4C/BOC-1$, $B_3O_4C/BOC-2$ and B_3O_4C photocatalyst in (a) aqueous dispersion (for DMPO- $\cdot OH$) and (b) methanol dispersion (for DMPO- $\cdot O_2^-$), under visible light irradiation. (★ label as (a) hydroxyl radicals and (b) superoxide radicals).

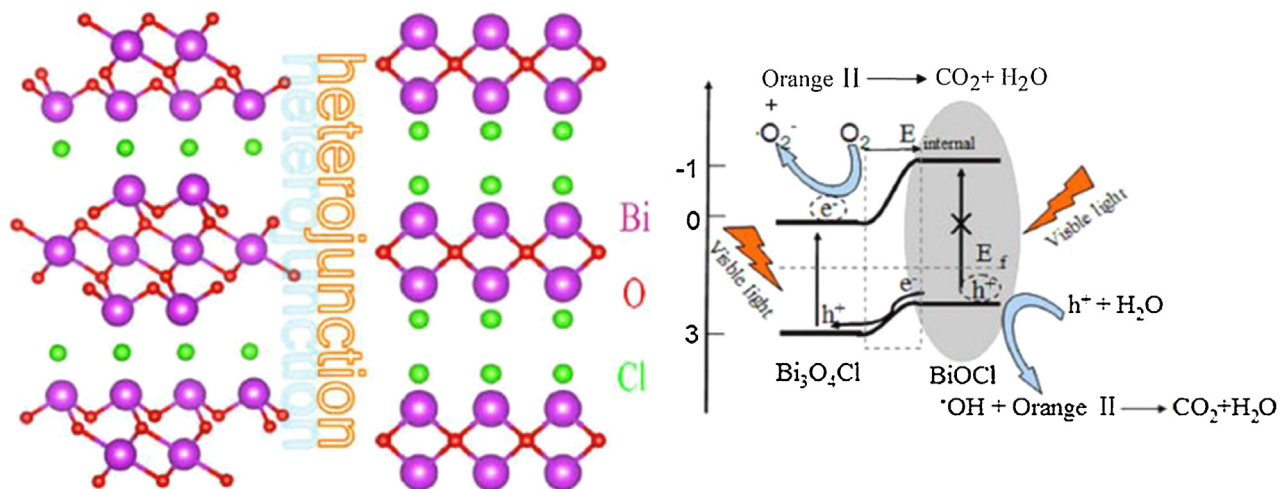


Fig. 10. Schematic diagram of the energy band structure of the B_3O_4C/BOC composite and the possible charge transfer process under visible light irradiation.

The VB maxima of both rods are at 2.39 eV and 2.94 eV, which is consistent with the above reported value (2.4 eV) of BOC and (2.97 eV) of B_3O_4C . The unchanged VB maximum therefore indicates that the conduction band (CB) minimum of BOC is lowered by 0.05 eV and B_3O_4C is raised by 0.01 eV with respect to Lee et al. [17] and Li et al. [24]. When B_3O_4C and BOC form a heterojunction after being closely joined together, an internal static electricfield ($E_{internal}$) is formed at their interface with the electricfield direction from B_3O_4C to BOC, so that the Fermi levels (E_f) equilibrate. As a consequence, a space charge region at the interface of the semiconductors formed because of electron migration and the bands of B_3O_4C and BOC will bend. Due to the VB level of B_3O_4C is lower by 0.57 V than that of BOC, unlike an A-type heterojunction, the B_3O_4C/BOC composite belongs to the “B-type heterojunction” class where holes are not generated on the nonactivated semiconductor in the heterojunction structure under visible-light irradiation [17–37]. According to the band gap of B_3O_4C and BOC, only B_3O_4C can be activated by visible light. Under visible light illumination, the electrons (e^-) in the VB of

B_3O_4C are excited to the CB and holes remains in the VB of B_3O_4C . The electrons in the VB of BOC may transfer to the VB of B_3O_4C because of the internal static electric field. Then the electrons in the CB of B_3O_4C are trapped by the O_2^- to form reactive $\cdot O_2^-$. At the same time, the h^+ left in VB in BOC can directly oxidize the organic compounds or react with H_2O to form $\cdot OH$ radicals. Thus, the photogenerated charge carriers are effectively separated by the internal field created by the B-type heterojunction between B_3O_4C and BOC and the photocatalytic activity is enhanced.

4. Conclusions

In summary, B_3O_4C/BOC plate-on-plate heterojunction photocatalyst was successfully synthesized via a simple one-pot hydrothermal method. The prepared hierarchical B_3O_4C/BOC composites showed an enhanced capacity to photocatalytic oxidation of Orange II compared with the pure BOC due to the efficient separation of photogenerated charge carriers, which was confirmed

by the results of electrochemical photocurrent and PL measurements. In addition, the photocatalytic mechanism studies indicated that •OH and •O²⁻ radicals are the main reactive species in this visible-light photocatalytic system, which resulted in a high mineralization efficiency for Orange II. With further improvement and optimization, the B₃O₄C/BOC heterojunction photocatalyst should offer some insight for the future development of technology applications to the degradation of dyes.

Acknowledgements

This work was financially supported by NSFC (Grants U1305242, Nos. 21373051 and 21173044), the great Science and Technology Project of Fujian Province of PR China (2012Y4003). The Project of Education Office of Fujian province (JK15002).

Appendix A. Supplementary data

Supplementary data associated with this article can be found, in the online version, at <http://dx.doi.org/10.1016/j.apcatb.2015.12.021>.

References

- [1] G.G. Briand, N. Burford, *Chem. Rev.* 99 (1999) 2601–2658.
- [2] M.L. Marin, L. Santos-Juanes, A. Arques, A.M. Amat, M.A. Miranda, *Chem. Rev.* 112 (2012) 1710–1750.
- [3] K. Nakata, T. Ozaki, C. Terashima, A. Fujishima, Y. Einaga, *Angew. Chem. Int. Ed.* 53 (2014) 871–874.
- [4] V.N. Kuznetsov, N. Serpone, *J. Phys. Chem. C* 113 (2009) 15110–15123.
- [5] H.L. Peng, C.K. Chan, S. Meister, X.F. Zhang, Y. Cui, *Chem. Mater.* 21 (2009) 247–252.
- [6] J. Ma, X. Liu, J. Lian, X. Duan, W. Zheng, *Cryst. Growth Des.* 10 (2010) 2522–2527.
- [7] K. Zhang, J. Liang, S. Wang, J. Liu, K. Ren, X. Zheng, H. Luo, Y. Peng, X. Zou, X. Bo, J. Li, X. Yu, *Cryst. Growth Des.* 12 (2012) 793–803.
- [8] H. Cheng, B. Huang, Y. Dai, *Nanoscale* 6 (2014) 2009–2026.
- [9] J. Li, Y. Yu, L.Z. Zhang, *Nanoscale* 6 (2014) 8473–8488.
- [10] R.S. Yuan, T. Chen, E.H. Fei, J.L. Lin, Z.X. Ding, J.L. Long, Z.Z. Zhang, X.Z. Fu, P. Liu, L. Wu, X.X. Wang, *ACS Catal.* 1 (2011) 200–206.
- [11] L. Zhang, W. Wang, S. Sun, D. Jiang, E. Gao, *Appl. Catal. B Environ.* 162 (2015) 470–474.
- [12] X. Zhang, Z.H. Ai, F.L. Jia, L.Z. Zhang, *J. Phys. Chem. C* 112 (2008) 747–753.
- [13] L. Kong, Z. Jiang, H.H.C. Lai, T. Xiao, P.P. Edwards, *Prog. Nat. Sci. Mater.* 23 (2013) 286–293.
- [14] R. Saraf, C. Shivakumara, S. Behera, H. Nagabhushana, N. Dhananjaya, *RSC Adv.* 5 (2015) 4109–4120.
- [15] J. Jiang, L. Zhang, H. Li, W. He, J.J. Yin, *Nanoscale* 5 (2013) 10573–10581.
- [16] H. Lin, L. Ding, Z. Pei, Y. Zhou, J. Long, W. Deng, X. Wang, *Appl. Catal. B Environ.* 160–161 (2014) 98–105.
- [17] S.Y. Chai, Y.J. Kim, M.H. Jung, A.K. Chakraborty, D. Jung, W.I. Lee, *J. Catal.* 262 (2009) 144–149.
- [18] L. Lei, H. Jin, Q. Zhang, J. Xu, D. Gao, Z. Fu, *Dalton. T.* 44 (2015) 795–803.
- [19] S. Shi, M.A. Gondal, A.A. Al-Saadi, R. Fajgar, J. Kupcik, X. Chang, K. Shen, Q. Xu, Z.S. Seddiggi, *J. Coll. Interface Sci.* 416 (2014) 212–219.
- [20] S. Shamaila, A.K. Sajjad, F. Chen, J. Zhang, *J. Coll. Interface Sci.* 356 (2011) 465–472.
- [21] S. Jiang, K. Zhou, Y. Shi, S. Lo, H. Xu, Y. Hu, Z. Gui, *Appl. Surf. Sci.* 290 (2014) 313–319.
- [22] X.P. Lin, T. Huang, F.Q. Huang, W.D. Wang, J.L. Shi, *J. Phys. Chem. B* 110 (2006) 24629–24634.
- [23] Q. Wang, J. Hui, Y. Huang, Y. Ding, Y. Cai, S. Yin, Z. Li, B. Su, *Mater. Sci. Semicond. Proc.* 17 (2014) 87–93.
- [24] A.K. Chakraborty, M.A. Kebede, *React. Kinet Mech. Catal.* 106 (2012) 83–98.
- [25] G. Tian, Y. Chen, W. Zhou, K. Pan, Y. Dong, C. Tian, H. Fu, *J. Mater. Chem.* 21 (2011) 887–892.
- [26] S.-T. Huang, Y.-R. Jiang, S.-Y. Chou, Y.-M. Dai, C.-C. Chen, *J. Mol. Catal. A Chem.* 391 (2014) 105–120.
- [27] F. Tian, Y. Zhang, G. Li, Y. Liu, R. Chen, *New J. Chem.* 39 (2015) 1274–1280.
- [28] K. Zhang, C. Liu, F. Huang, C. Zheng, W. Wang, *Appl. Catal. B Environ.* 68 (2006) 125–129.
- [29] L. Cai, T. Xu, J. Shen, W. Xiang, *Mater. Sci. Semicond. Proc.* 37 (2015) 19–28.
- [30] D. Sun, J. Li, L. He, B. Zhao, T. Wang, R. Li, S. Yin, Z. Feng, T. Sato, *Cryst. Eng. Commun.* 16 (2014) 7564.
- [31] (a) W. Xiong, Q. Zhao, X. Li, D. Zhang, *Catal. Commun.* 16 (2011) 229–233;
 (b) X.Y. Zhang, H.P. Li, X.L. Cui, Y.H. Lin, *J. Mater. Chem.* 20 (2010) 2801–2806;
 (c) Y. Chen, G. Tian, Y. Shi, Y. Xiao, H. Fu, *Appl. Catal. B Environ.* 164 (2015) 40–47;
 (d) J. Zhou, G. Tian, Y. Chen, X. Meng, Y. Shi, X. Cao, K. Pan, H. Fu, *Chem. Commun. (Camb.)* 49 (2013) 2237–2239.
- [32] L. Junqi, Z. Zhenfeng, G. Zhanyun, W. Yu, *Micro. Nano Lett.* 9 (2014) 65–68.
- [33] D. Yue, D. Chen, Z. Wang, H. Ding, R. Zong, Y. Zhu, *Phys. Chem. Chem. Phys.* 16 (2014) 26314–26321.
- [34] H. Xu, C. Wang, Y. Song, J. Zhu, Y. Xu, J. Yan, Y. Song, H. Li, *Chem. Eng. J.* 241 (2014) 35–42.
- [35] J. Cao, B. Xu, B. Luo, H. Lin, S. Chen, *Catal. Commun.* 13 (2011) 63–68.
- [36] J. Xu, W. Wang, S. Sun, L. Wang, *Appl. Catal. B Environ.* 111–112 (2012) 126–132.
- [37] Z. He, Y. Shi, C. Gao, L. Wen, J. Chen, S. Song, *J. Phys. Chem. C* 118 (2014) 389–398.
- [38] Y.Q. Lei, G.H. Wang, S.Y. Song, W.Q. Fan, H.J. Zhang, *Crystengcomm* 11 (2009) 1857–1862.
- [39] W.L.W. Lee, S.T. Huang, J.L. Chang, J.Y. Chen, M.C. Cheng, C.C. Chen, *J. Mol. Catal. A Chem.* 361 (2012) 80–90.
- [40] L.A. Perez-Estrada, A. Aguera, M.D. Hernando, S. Malato, A.R. Fernandez-Alba, *Chemosphere* 70 (2008) 2068–2075.
- [41] S.M. Wang, D.L. Li, C. Sun, S.G. Yang, Y. Guan, H. He, *Appl. Catal. B Environ.* 144 (2014) 885–892.
- [42] H.W. Huang, X.W. Li, J.J. Wang, F. Dong, P.K. Chu, T.R. Zhang, Y.H. Zhang, *ACS Catal.* 5 (2015) 4094–4103.
- [43] Z. Nie, Q. Tian, Y.P. Liu, Y. Liu, *Magn. Reson. Chem.* 44 (2006) 38–44.
- [44] B. Gao, A.K. Chakraborty, J.M. Yang, W.I. Lee, *B Kor. Chem. Soc.* 31 (2010) 1941–1944.
- [45] X.W. Huang, H.F. Chen, *Appl. Surf. Sci.* 284 (2013) 843–848.